Alkali Metal Cations Influence the CO 2 Adsorption Capacity of Nanosized Chabazite: Modeling vs Experiment

Sajjad Ghojavand, Benoit Coasne, Edwin Clatworthy, Rémy Guillet-Nicolas, Philippe Bazin, Marie Desmurs, Luis Jacobo Aguilera, Valérie Ruaux, Svetlana Mintova, Valérie Ruaux

Alkali Metal Cations Influence the CO_2 Adsorption Capacity of Nanosized Chabazite: Modeling *vs* Experiment

Sajjad Ghojavand[a], Benoit Coasne[b*], Edwin B. Clatworthy[a], Rémy Guillet-Nicolas[a], Philippe Bazin[a], Marie Desmurs[a], Luis Jacobo Aguilera[a], Valérie Ruaux[a], Svetlana Mintova[a*]

[a] Normandie Université, ENSICAEN, UNICAEN, CNRS, Laboratoire Catalyse et Spectrochimie (LCS), 14000 Caen, France

[b] Université Grenoble Alpes, CNRS, Laboratoire Interdisciplinaire de Physique (LIPhy), 38000 Grenoble, France

Abstract:

The CO_2 adsorption behavior of nanosized chabazite (CHA) containing different compositions of extra-framework alkali metal cations (Na^+, K^+, Cs^+) with a constant Si/Al ratio of 2.2 was investigated experimentally (adsorption isotherms and *in situ* FTIR spectroscopy) and theoretically by Grand Canonical Monte Carlo (GCMC) modeling. The CO_2 adsorption isotherms were in a good agreement with the GCMC modeling in the pressure range of 0–60 KPa for all samples except the Cs^+ containing nanosized CHA. The GCMC modeling did not consider the kinetics of adsorption thus the CO_2 capacity for the Cs-CHA sample was overestimated; the partial blockage of the pores and inaccessibility of CO_2 to the free voids of the CHA structure was experimentally observed by recording adsorption isotherms and *in situ* FTIR study. The FTIR results revealed the CO_2 adsorbed mainly physically on all samples with the sorption capacity decreasing in the following order: Na-CHA ≃ K-CHA > Cs-CHA. The Na-CHA demonstrated significant micropore volume compared to the other samples as measured by N_2 physisorption due to the inability of Na^+ to effectively occupy the 8MRs. This study implies that the different alkali metal cation forms of the nanosized CHA zeolite are of practical interest for flue gas purification where a high CO_2/N_2 selectivity is required.

Keywords: nanozeolite, chabazite, CO_2 adsorption, extra-framework cations, gas separation, heat of adsorption

*Corresponding author. E-mail address: svetlana.mintova@ensicaen.fr

Tel: +33231452737

1. Introduction

Since the industrial revolution the concentration of atmospheric CO_2 has been continuously increasing.[1] Recent research shows that this value has increased from 280 ppm to approximately 400 ppm in the last two centuries, which is responsible for the current increase in average global temperatures.[2] As a result, capturing CO_2 emitted from various industries in the form of flue gas (3–20% CO_2, 65–80% N_2) is a key strategy to reduce anthropogenic global warming and has received significant attention.[3–6] Four technologies are currently employed for CO_2 capture: absorption with amine-based solvents, adsorption by nanoporous solids, cryogenic distillation, and membranes.[7] Adsorption of CO_2 by nanoporous materials is a widely used and attractive technology due to its ease of operation, use of non-corrosive materials, and low energy requirement (specially compared to amine-based absorption).[8–12]

Zeolite-based adsorbents are advantageous compared to other porous materials due to their non-toxic nature, high thermal stability, high selectivity dictated by their structure and chemical composition, and affordability.[13,14] Conventional zeolites, which have particle sizes in the order of micrometers, are composed of aggregates of individual crystals.[15] As a result, micron-sized zeolites suffer from diffusion limitations of guest molecules through their pore networks, however, this can be addressed by decreasing the zeolite particle size.[16] Nanozeolites are typically composed of discrete particles (single crystals) which possess a greater external surface area and number of available active sites compared to micron-sized zeolites.[17,18]

Zeolites can be divided into different categories based on their pore sizes; small (3.0–4.5 Å), medium (4.5–6 Å), large 6.0–8.0 Å), and extra-large (> 8.0 Å).[19] Small-pore zeolites are suitable candidates for CO_2 capture from N_2-containing mixtures; the kinetic diameters of these small molecules is similar (3.3 and 3.6 Å for CO_2 and N_2 respectively). The CO_2 capacity of different zeolites is already reviewed by Cheung and Hedin,[20] revealing that among the known zeolites the CHA has the highest CO_2 capacities.[20] In addition, the size and shape of the 8-membered rings (8MRs) of the CHA zeolite which control the access to the zeolite pore network can be controlled by the presence of different extra-framework cations (EFCs) and adsorbates.[19,21–24] Two mechanisms for the selective adsorption of CO_2 on small-pore zeolites have been proposed: molecular sieving due to the differences between the zeolite pore size and molecule kinetic diameter, and window-keeping mechanism by extra-framework cations (EFCs).[25] The latter, described by Shang *et al.* as molecular trapdoor behavior, occurs due to the occupation of the zeolite 8MRs by EFCs which control access to the zeolite pore network whereby the EFCs reject or admit different guest molecules based on their interactions with them.[23,26] They showed that the CO_2 guest molecules induced the door-keeper EFCs to move out from the center of 8MRs of the zeolite and selectively admit CO_2 to the CHA supercages compared to non-polar molecules such as

N_2 and CH_4.[23,24,26] Using thermogravimetric analysis (TGA), we reported selective adsorption of CO_2 over CH_4 due to molecular trapdoor behavior by a nanosized CHA sample (crystal sizes ~ 190 nm) containing a mixture of alkali metal cations (Na^+, K^+, Cs^+).[27] In that work, the presence of Cs^+ located in the 8MR of the CHA structure was identified as the cation responsible for the selective adsorption of CO_2 evidenced by its ability to displace about the 8MR aperture in the presence of CO_2.[27]

The CHA structure is described by a three-dimensional pore system containing supercages of 6.7 × 10 Å (*t-cha*) which are accessed by six 8MRs of 3.8 × 3.8 Å connected along the c-axis by double six-membered rings (*d6r*s).[27] Four EFC sites exist in the CHA framework (Fig. 1a): at the center of a *d6r* prism (SI), at the triad axis of a *d6r* prism but displaced inside the *t-cha* (SII), in the *t-cha* at the corner of a four-ring window of a *d6r* (SIII), and at the center of an 8MR window (SIII').[27–29]

Recently we demonstrated the one-pot synthesis of CHA zeolite with small nanocrystals (< 60 nm) using only alkali metal cations (Na^+, K^+, and Cs^+) as inorganic structural-directing agents, and their behavior during the crystallization stage was studied.[30] Zhang *et al.* have reported on the CO_2 adsorption capacity and separation performance of alkali (Li^+, Na^+, and K^+) and alkaline-earth (Mg^{2+}, Ca^{2+}, Ba^{2+}) metal containing micron-sized CHA zeolites in flue gas streams. From adiabatic simulation calculations it was found that the Na- and Ca-containing CHA zeolites possess advantages for high temperature separation of CO_2 compared to NaX due to their greater capture defined by the product of their adiabatic working selectivity and capacity.[7]

Here we describe the preparation of four different cationic forms of nanosized CHA with different alkali metal compositions as EFCs (Na^+, K^+, Cs^+, and mixed) with a crystal size of 60 nm and Si/Al ratio of 2.2. The CO_2 adsorption capacity of the CHA nanocrystal samples was predicted using Grand Canonical Monte Carlo (GCMC) calculations and was compared to the experimental results from adsorption isotherm measurements and *in situ* FTIR spectroscopy. Good agreement was observed between the modelling and experimental methods when the EFCs do not cause pore blockage demonstrating that GCMC is a powerful tool for predicting zeolite CO_2 adsorption capacities. Experimental CO_2 adsorption measurements showed a higher CO_2 capacity for nanosized K-CHA compared to the micron-sized K-CHA. Following the adsorption of CO_2 on the nanosized zeolite samples using *in situ* FTIR revealed that CO_2 adsorbs mainly by physisorption on all of the samples which was highlighted by three consecutive regeneration cycles by vacuum after CO_2 dosing. The results clearly demonstrated that the CHA nanocrystals are prospective candidates for CO_2 separation from N_2 in vacuum swing applications.

2. Experimental and modeling section

2.1. Materials and synthesis of CHA nanocrystals

All reagents were used as received unless otherwise specified. Sodium hydroxide pellets (98 wt%), sodium chloride (99 wt%), potassium hydroxide (85 wt%), potassium chloride (99.5 wt%), LUDOX AS-40, and sodium aluminate ($NaAlO_2$, 40–45% Na_2O, 50–56% Al_2O_3) were purchased from Sigma-Aldrich. Cesium hydroxide hydrate (15–20 wt% H_2O), and cesium chloride (99.5 wt%) were purchased from Alfa Aesar. Double distilled (dd) water prepared by an Aquatron water still A4000D was used for all syntheses. The synthesis of the CHA nanozeolite has been described previously.[30] 0.54 g of $NaAlO_2$ was mixed with 4.2 g of water under rapid stirring. After dissolution, 1.7 g of NaOH, 0.824 g of KOH, and 0.442 g of CsOH (50 wt.% Cs in water) were added and stirred for 2 hours to obtain a clear solution. Then, 10 g of LUDOX AS-40 was added dropwise under vigorous stirring. The final composition of the alkali aluminosilicate colloidal suspension was 0.2 Cs_2O: 1.5 K_2O: 6.0 Na_2O: 16.0 SiO_2: 0.7 Al_2O_3: 141.7 H_2O. The alkali aluminosilicate colloidal suspension was then aged under vigorous stirring at room temperature for 17 days followed by hydrothermal treatment in a static oven at 90 °C for 7 hours. The CHA nanocrystals were recovered by centrifugation and washed with hot water (90 °C) until a neutral pH (7–8) of the decanted solution was achieved. The recovered CHA nanocrystals were dried in an oven at 60 °C overnight and the final as-prepared CHA nanocrystals were labeled as AP-CHA.

AP-CHA was ion-exchanged to obtain different alkali-metal cation forms as described: 10 mL of 1 M NaCl, KCl, or CsCl was added to 250 mg of AP-CHA (liquid/solid ratio of 40), and the mixture was stirred for 2 hours. Afterwards, the different alkali-metal forms of CHA nanocrystals were recovered by centrifugation and washed with water three times. This procedure was repeated three times and the recovered CHA nanocrystals were dried in an oven at 60 °C overnight. The ion-exchanged samples with Na^+, K^+ and Cs^+ were labeled as Na-CHA, K-CHA, and Cs-CHA, respectively.

2.2. Characterization techniques

Powder X-ray diffraction (PXRD) patterns were collected with a PANalytical X'Pert Pro diffractometer using Cu-Kα1 radiation (λ = 1.5406 Å, 45 kV, 40 mA). Inductively coupled plasma mass spectrometry (ICP-MS) measurements were performed using a 7900 ICP-MS from Agilent Technologies. Magic-angle spinning nuclear magnetic resonance (MAS NMR) spectra of ^{29}Si nuclei were recorded with a single pulse on a Bruker Avance 500 MHz (11.7 T) spectrometer using 4 mm-OD zirconia rotors with a spinning frequency of 12 kHz. Single pulse excitation (30° flip angle) of 3 µs was used for ^{29}Si MAS NMR experiment and 30 s of recycle delay. Tetra-methylsilane (TMS) was used as a reference for ^{29}Si nuclei.

N_2 adsorption and desorption isotherms were recorded at 77 K and CO_2 adsorption isotherms recorded at various temperatures (248, 283 and 298 K) were measured on a Micromeritics 3Flex Surface Characterization unit (Norcross, GA, USA). The samples were outgassed under vacuum at 623 K for at least 8 h prior to measurement. The specific surface area was calculated using the Brunauer-Emmet-Teller (BET) equation and following the procedure described by Rouquerol *et al.*[31] Micropore volumes were determined by applying an advanced NLDFT method assuming N_2 adsorption at 77 K in cylindrical siliceous zeolite micropores. Isosteric heat of adsorption calculations were computed based on the Clausius-Clapeyron equation applied to CO_2 adsorption isotherms between 248 and 298 K using the ASiQwin 5.2 software provided by Quantatec (Anton Paar, Boynton Beach, FL, USA). [32,33] Thermogravimetric analysis (TGA) was performed using a Setsys SETARAM analyzer. The cycling experiments were performed under heating in the presence of Ar and flowing CO_2 from 298 to 623 K (heating rate of 10 K min^{-1}) and held at 623 K for 1.5 hours under Ar, followed by cooling down to 298 K (cooling rate of 20 K min^{-1}), followed by flowing CO_2 (40 mL min^{-1}) for 2 hours.

In situ FTIR spectroscopic measurements of zeolite samples were performed on a self-supported pellet (~20 mg and a diameter of 16 mm); the transmission spectra were recorded with a Thermo Scientific Nicolet iS50 FTIR spectrometer equipped with an MCT detector, at a spectral resolution of 4 cm^{-1}. The infrared cell used here for the CO_2 adsorption isotherm experiments is the Carroucell, an *in situ* cell recently developed at the LCS laboratory for concomitant multi-samples analyzes.[34] The specificity of this cell is to be able to accommodate 12 samples simultaneously in a single chamber (same experimental conditions for all samples). While, two of the sample positions can be left unoccupied in order to be able to perform a background or an IR spectrum of the gas phase. The Carroucell IR-cell is equipped with a heating element in order to activate the samples at 623 K prior to the measurements. The cell was connected to a pumping system for the treatment under high vacuum (up to 10^{-6} kPa). The samples were activated by heating with a ramp rate of 3 K min^{-1} followed by heating at 623 K for 4 h under high vacuum. All IR spectra relating to CO_2 adsorption were recorded at room temperature. The molar absorption coefficients used in this work to obtain the physisorption and chemisorption isotherms were 16 and 40 cm μmol^{-1}, respectively.[35,36]

2.3. Grand Canonical Monte Carlo calculations of CO_2 adsorption in CHA zeolite

To model the CHA unit cell the structure published by Debost *et al.* was employed.[27] The unit cell was multiplied three times in each direction (x, y, and z) to create a super cell consisting of 27 unit cells upon which all the molecular modeling calculations were performed. For this study, following previous work[37,38], the Al atoms in the CHA samples were randomly distributed while

respecting Löwenstein's rule[39] and the position of cations were chosen next to the negatively charged Al tetrahedra.

The forcefield parameters used in this work to model the interactions between the alkali cations, the rigid zeolite framework, and the CO_2 molecules are those derived by Jeffroy *et al.* and summarized in Table 1.[40] All interactions between the cations and the framework oxygens ($O_{zeolite}$) were considered as Buckingham interactions. Lennard-Jones interactions were considered for the rest of the atom pairs and the Lorentz-Berthelot combination rules [$\sigma_{ij} = (\sigma_{ii} + \sigma_{jj}) / 2$ and $\varepsilon_{ij} = (\varepsilon_{ii} \times \varepsilon_{jj})^{0.5}$] were used to estimate forcefield parameters for different atom pairs.

Table 1. Force field parameters used in this work

	Lennard-Jones: $-4\varepsilon[\sigma^6/r^6 - \sigma^{12}/r^{12}]$		
	σ / Å	**ε / K**	**q / e**
C	2.757	28.13	+0.6512
O	3.033	80.51	-0.3256
Na	2.586	50.27	+1
K	2.820	62.00	+1
Cs	3.165	59.72	+1
$O_{zeolite}$	3.000	93.53	-0.8308
$Al_{zeolite}$	-	-	+1.1900
$Si_{zeolite}$	-	-	+1.3837
	Buckingham: $\alpha \exp(-\beta r) - \gamma / r^6$		
	α / K	**β / Å^{-1}**	**γ / K Å^6**
Na ⋯ $O_{Zeolite}$	6.11×10^7	4.05	7.652×10^5
K ⋯ $O_{Zeolite}$	6.11×10^7	3.53	1.800×10^5
Cs ⋯ $O_{Zeolite}$	6.11×10^7	3.20	2.831×10^5

The GCMC simulations of CO_2 adsorbed at 248, 273, and 298 K in CHA nanozeolite samples with different cations were performed consistent with the chemical compositions determined with ICP-MS (see Table 2). The GCMC technique is a stochastic method that simulates a system having a constant volume V (the pore with the adsorbed phase), in equilibrium with an infinite reservoir of particles imposing its chemical potential μ_{CO2} for the adsorbed species and its temperature T. The absolute adsorption isotherm is given by the ensemble average of the number of each adsorbate molecule as a function of the CO_2 fugacities (f_{CO2}) of the reservoir (the latter are determined from the chemical potential μ).

3. Results and Discussion

The CHA nanocrystals containing different alkali metal cations were characterized by PXRD, ICP-MS, and ^{29}Si MAS NMR and the results are presented in Fig. 1b, Table 2, and Fig. S1, respectively. All ion-exchanged samples contain a small content of co-cations (K and/or Cs) in the CHA unit cell (Table 2). The different alkali forms of CHA show minor differences in XRD patterns (Fig. 1b). For instance, the intensity of the Bragg peak at 26.62 °2θ with hkl of (2 0 -1) and (2 -1 0) is more intense in the Na-CHA sample.[41] Another example is the diffraction peak at 9.48 °2θ with hkl value of (1 0 0) disappears in the XRD pattern of Cs-CHA sample, while two diffraction peaks at 16.02 and 19.02 °2θ with hkl of (1 -1 1) and (2 0 0), respectively appear only in this sample.[41] Nevertheless, all the different reflections in the XRD patterns presented in Fig. 1b are attributed to CHA framework.[41] Panezai *et al.*[42] reported similar results for zeolite X in different cationic forms (Li^+, Na^+, Ca^{2+}).

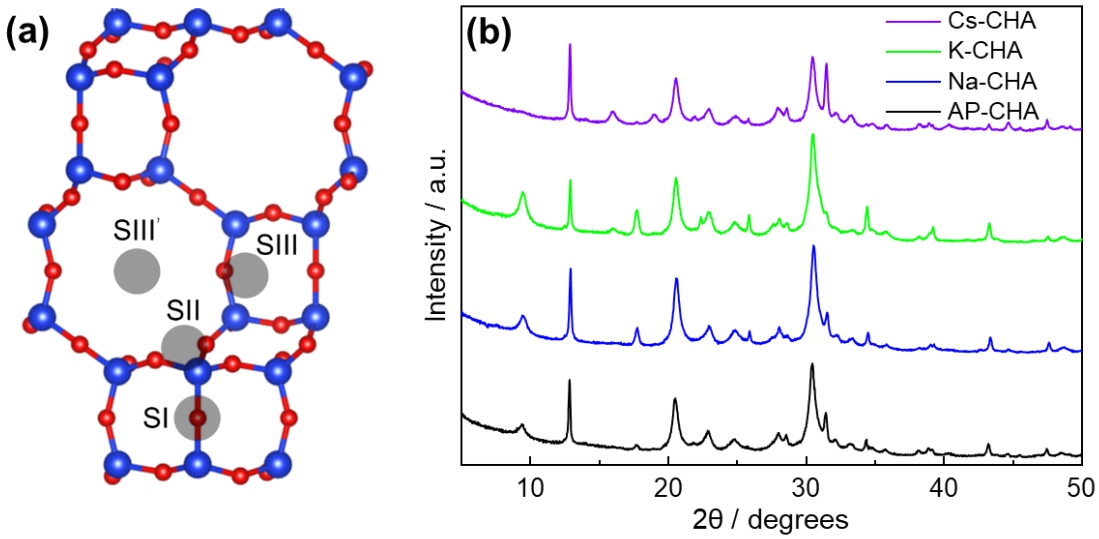

Fig. 1 (a) Schematic representation of CHA atomic structure and the occupancy sites for extra-framework cations (hollow grey spheres). Four types of cation sites exist: at the center of a *d6r* (SI); above a *d6r* inside the cavity (SII); next to a 4MR of a *d6r* inside the cavity (SIII); at the center of an 8MR (SIII'); T atoms (Si, Al) are depicted by blue spheres, and oxygen atoms by red. (b) XRD patterns of the nanosized AP-CHA, Na-CHA, K-CHA, and Cs-CHA zeolite samples.

Table 2. Chemical composition and Si/Al ratio of nanosized AP-CHA, Na-CHA, K-CHA, and Cs-CHA samples.

Sample	Chemical formula (ICP-MS)	Si/Al (^{29}Si MAS NMR)
AP-CHA	$Na_{1.8}K_{5.7}Cs_{4.0}Al_{11.1}Si_{24.8}O_{72}$	2.2

Na-CHA	$Na_{7.3}K_{1.0}Cs_{2.3}Al_{10.6}Si_{25.4}O_{72}$	2.1
K-CHA	$K_{10.4}Cs_{1.0}Al_{11.4}Si_{24.9}O_{72}$	2.2
Cs-CHA	$K_{1.8}Cs_{10.5}Al_{11.7}Si_{24.2}O_{72}$	2.1

The CO_2 adsorption isotherms predicted for the CHA nanocrystals with different cations using GCMC calculations at 248, 273, and 298 K are presented in Fig. 2. The GCMC results reveal that the CO_2 capacity of the CHA nanozeolite decreases upon increasing the size of extra-framework alkali metal cations (Na^+, K^+, and Cs^+). This is expected as less free space is available in the CHA cages occupied by larger cations.

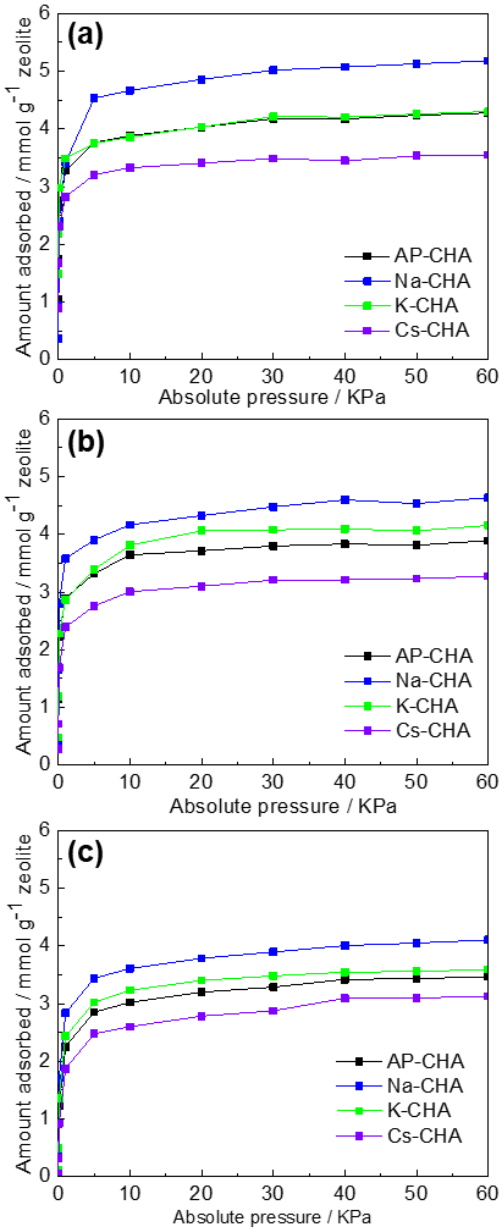

Fig. 2 CO_2 adsorption isotherms of nanosized AP-CHA, Na-CHA, K-CHA, and Cs-CHA zeolite samples at (a) 248 K, (b) 273 K, and (c) 298 K calculated using the GCMC method.

The experimentally measured adsorption isotherms of CO_2 on the CHA nanocrystals at the same temperatures (248, 273, and 298 K) as the GCMC modelling are presented in Fig. 3. All CO_2 isotherms were fully reversible; the adsorption curves associated with less potential cumulative errors are presented in Fig.3. Similar to the GCMC results, increasing the adsorption temperature was found to lead to a decrease in the CO_2 adsorption capacity of the CHA nanocrystals. However, unlike the GCMC results the K-CHA sample shows similar CO_2 adsorption behavior to the Na-CHA sample, as well as the highest CO_2 adsorption capacity. Nanosized Na-CHA and Cs-CHA samples showed CO_2 capacities of 4.5 and 2.1 mmol g^{-1} respectively at 60 KPa and 273 K which is similar to their micron-sized counterparts.[7,23] While in the nanosized K-CHA sample an increase of CO_2 capacity was observed compared to the micron-sized K-CHA counterpart (4.5 *vs* 4.1 mmol g^{-1} at 60 KPa and 273 K).[24] The experimentally measured CO_2 adsorption capacity for the nanosized CHA samples decreases in the following order: Na-CHA ≃ K-CHA > AP-CHA > Cs-CHA (Fig. 3). To address the effect of small amounts of co-cations in the nanosized CHA samples, the CO_2 adsorption capacity at 50 kPa of CO_2 and 273 K *vs* the amount of alkali EFCs (i.e. Na^+, K^+, and Cs^+) in the different nanosized alkali forms of CHA is presented (Fig. S2). As shown in Fig. S2c, the CO_2 capacity is linearly influenced by the Cs amount present in the CHA. By increasing the content of Cs^+ EFC (ionic diameter of 3.4 Å) more space within the CHA framework is occupied and hence, the overall CO_2 capacity decreases.[43] While such correlations are not seen for the samples with increased amount of Na^+ and K^+ EFCs with ionic diameters of 1.9 and 2.7 Å, respectively[43] (Fig. S2a,b). The CO_2 adsorption capacity is significantly higher (over 4 mmol g^{-1} at 50 kPa and 273 K) for Na-CHA, K-CHA, and AP-CHA samples compared to the Cs-CHA sample (2 mmol g-1 at 50 kPa and 273 K). This suggests that the Cs content strictly restrict the access of CO_2 to the adsorption sites. Moreover, the nanosized Cs-CHA sample show a significantly lower experimentally measured CO_2 adsorption capacity as compared to the other samples and to the theoretically predicted values by GCMC (Fig. 2 *vs* Fig. 3). Such discrepancies are discussed in more detail bellow. GCMC calculations are an effective tool to predict CO_2 adsorption in different CHA zeolite samples. However, perfect zeolite crystals without defects are used to describe the zeolite structure and adsorbate. Inconsistencies between experimentally measured and theoretically calculated results may arise from the fact that the defects in zeolites effect the adsorption of CO_2. Additionally, large EFCs such as Cs^+ located within the zeolite pores can affect the CO_2 diffusion to the adsorption sites while GCMC calculations do not take into consideration these diffusion limitations. In the case of the nanosized Cs-CHA sample, all SIII' sites in the 8MRs are occupied by Cs^+ EFCs and the remaining Cs^+ and K^+ EFCs most likely occupying the SII sites (see cationic sites in Fig. 1a).[27–29,44] The occupation of the SII site by Cs^+ would significantly decrease the available space within the CHA cages due to the cation

size, however, those free spaces are available for the GCMC simulations and resulted in overestimation of CO_2 adsorption capacities comparing to the experimental adsorption measurements (Fig. 2 *vs* Fig. 3).

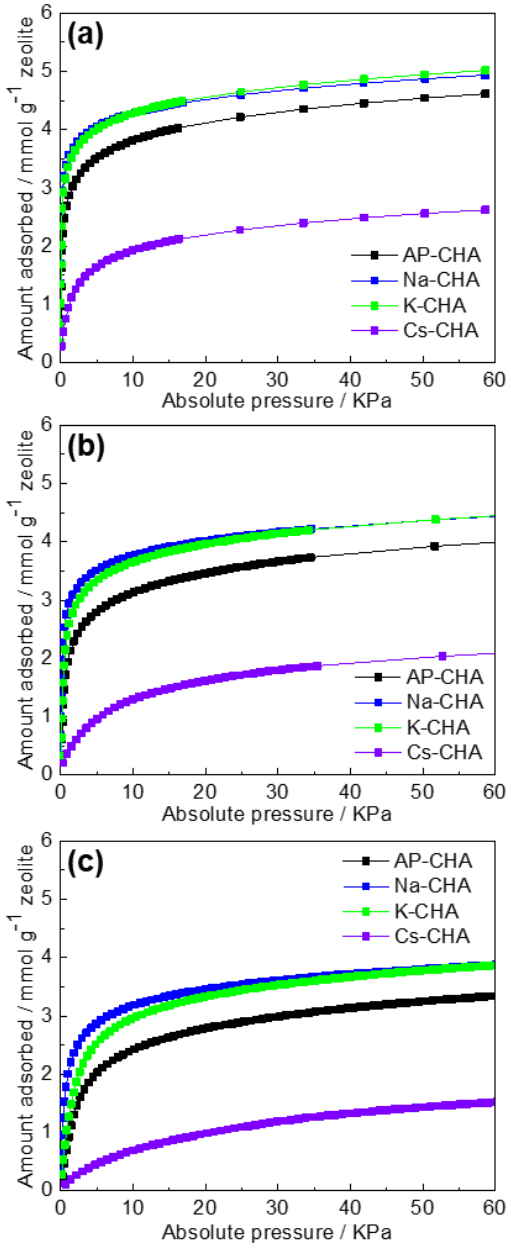

Fig. 3 CO_2 adsorption isotherms for nanosized AP-CHA, Na-CHA, K-CHA, and Cs-CHA zeolite samples measured at (a) 248 K, (b) 273 K, and (c) 298 K.

The N_2 adsorption and desorption isotherms of nanosized CHA samples with different cations measured at 77 K are presented in Fig. 4; the corresponding specific BET surface area and micropore volume are summarized in Table 3. In samples K- and Cs-CHA, all Na^+ cations were removed and replaced by the bigger and heavier K^+ and Cs^+ cations which occupy the SIII' positions

acting as door-keepers and prevent the diffusion of N_2 molecules efficiently inside the network at 77 K (Table 2). This phenomenon is not observed for sample Na-CHA with higher BET surface areas (439 m^2 g^{-1}). The nanosized AP-, K-, and Cs-CHA zeolite samples exhibit a low micropore volume (0.01 cm^3 g^{-1}) compared to the Na-CHA sample (0.14 cm^3 g^{-1}). This value is comparable to that of micron-sized Na-CHA with a similar Si/Al ratio and similar EFC composition reported by Ridha *et al.*[45] In the case of the nanosized Na-CHA sample, a small difference between the GCMC and experimental results is observed (Fig. 2 *vs* Fig. 3). This can be explained with the presence of co-cations (K^+ and Cs^+) in the sample determined experimentally (Table 2). The Na-CHA sample has a significantly higher micropore volume compared to the AP-, K- and Cs-CHA samples due to the preference of Na^+ occupying the SII site within the supercage (Fig. 4 and Table 3).[46] This behavior is consistent with the results reported previously for micron-sized Na-CHA with similar Si/Al ratios.[24,45] The observation of a high micropore volume and BET surface area determined by N_2 adsorption analysis at 77 K as well as a high CO_2 adsorption capacity measured at 273 K for the nanosized Na-CHA indicates that the sample does not exhibit molecular trapdoor behavior. For the nanosized K-CHA sample the GCMC results (Fig. 2) are in good agreement with the experimental adsorption isotherms (Fig. 3). The observation of a low micropore volume determined by N_2 adsorption analysis at 77 K and a high CO_2 adsorption capacity measured at 273 K for the nanosized K-CHA indicates that the sample exhibits molecular trapdoor behavior, consistent with the observations reported previously for micron-sized K-CHA.[23,24] The discrepancy between the experimental and theoretical results for the nanosized Cs-CHA sample can be explained by the restricted accessibility of CO_2 guest molecules to the CHA cages due to the presence of Cs^+ EFCs (*vide supra*). In the GCMC calculations, CO_2 molecules can be inserted and displaced freely subject to the available cavities in order to minimize the grand potential of the system at a given chemical potential (or fugacity) and temperature. However, in real samples, a significant part of the structure is inaccessible due to the presence of large Cs^+ cations. As a consequence, the theoretical results deviate from the experimental data for this specific case (Cs-CHA). The modeled CO_2 adsorption isotherm of the AP-CHA sample was calculated with respect to the experimentally determined chemical composition (see Table 2). As shown (Fig. 2 *vs* Fig. 3), the modeled and experimental CO_2 adsorption isotherms for the AP-CHA nanocrystals are in a good agreement. The good agreement can be explained by the low Cs^+ content in this sample (Table 2).

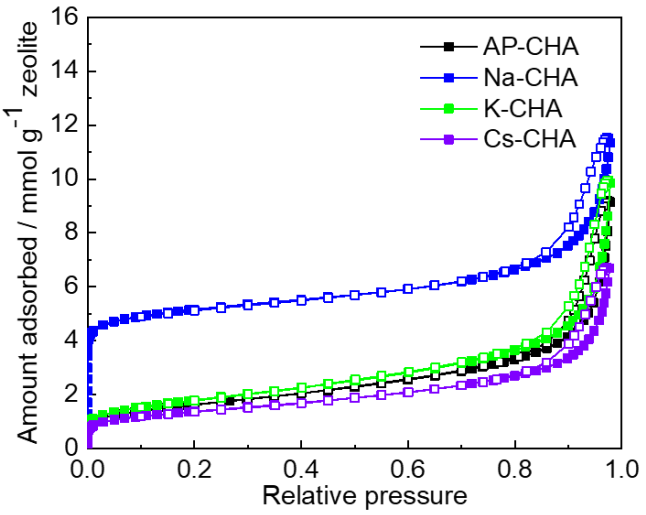

Fig. 4 Nitrogen adsorption/desorption isotherms of nanosized AP-CHA, Na-CHA, K-CHA, and Cs-CHA zeolite samples measured at 77 K (the filled squares represent the adsorption branch while the empty squares represent the desorption branch of the experiments).

Table 3. BET specific surface area and micropore volume of nanosized AP-CHA, Na-CHA, K-CHA, and Cs-CHA zeolite samples determined from N_2 adsorption measurements at 77 K and the corresponding CO_2 capacities measured at 50 kPa CO_2 at 273 K.

Sample	S_{BET} / m^2 g^{-1}	V_{micro} / cm^3 g^{-1}	CO_2 capacity* / mmol g^{-1}
AP-CHA	132	0.01	4.0
Na-CHA	439	0.14	4.5
K-CHA	146	0.01	4.5
Cs-CHA	111	0.01	2.1

* At 60 kPa of CO_2 and 273 K.

In order to better understand the interaction of the CO_2 molecules with the different EFCs, the isosteric heats of CO_2 adsorption (ΔH_{iso}) for the CHA nanocrystals were calculated as a function of CO_2 uptake by applying the Clausius-Clapeyron equation to the experimentally measured CO_2 adsorption isotherms between 248 to 298 K (Fig. 5).[32,33] Between the four different nanosized CHA samples, three different types of ΔH_{iso} behavior can be distinguished due to the different EFC content. (i) For nanosized AP- and K-CHA, the heat of adsorption initially increases slightly from 37.9 kJ mol^{-1} at 0.3 mmol g^{-1} loading to 38.7 and 40.8 kJ mol^{-1} at 1.6 mmol g^{-1} of CO_2 surface coverages, which is consistent with the presence of specific heterogeneous cationic adsorption sites interacting with the quadrupole moment of the CO_2 molecules (*i.e.* strong adsorbate-adsorbent interactions). As the amount of adsorbed CO_2 increases, steric (*i.e.* repulsive) adsorbate–adsorbate interactions become more substantial resulting in ΔH_{iso} slow decrease to lower values (around 30–35 kJ mol^{-1}). Eventually, a slow decreasing asymptote-like decay is

observed. This ΔH_{iso} behavior is well understood and documented for small pore zeolites.[47] The similar ΔH_{iso} values for AP- and K-CHA samples is likely a consequence of the similar cations location within the CHA structure; Cs^+ and K^+ prefer to occupy the SIII' site in the 8MR while the remaining Na^+ and K^+ occupy the SII site above the S6R. This provides similar coordination environments for CO_2 which will preferentially orientate along the c-axis (dual-cation site) as discussed by Pham *et al.* for CHA zeolite with a high Al content.[48] Previously we showed that the adsorbed CO_2 was coordinated along the c-axis of the supercage in high Al-containing nanosized CHA.[27] (ii) The Cs-CHA sample shows an almost constant ΔH_{iso} value with CO_2 loading. This sample reaches almost immediately a balance between decreasing adsorbate-adsorbent and increasing attractive adsorbate-adsorbate interactions at a ΔH_{iso} of about 35 kJ mol^{-1}. A small decrease to lower ΔH_{iso} (34.1 kJ mol^{-1}) is observed at higher coverages (1.7 mmol g^{-1}) and compared to K-CHA, access to the pore network of Cs-CHA is more restricted. This is due to the larger size of the Cs^+ EFCs which can interact more strongly with the framework oxygens of the 8MRs, as well as Cs^+ located at the SII site in the CHA cage, restricting the deviation of Cs^+ from the 8MR to allow the rapid uptake of CO_2.[23,26] The lower ΔH_{iso} value of Cs-CHA compared to K-CHA is likely due to the lower charge density of Cs^+ compared to K^+ despite the presumably shorter coordination distance for CO_2 at the dual-cation site, *i.e.* coordination between cations at either the SII/SII or SII/SIII' sites.[48] The almost constant ΔH_{iso} is likely due to the limited number of CO_2 molecules reaching the CHA supercage, resulting in an overall low adsorption uptake with a fast equilibrium followed. This is followed by a minor decrease of ΔH_{iso} values at higher coverages due to repulsive adsorbate−adsorbate interactions. For sample Cs-CHA, the cation reversible position deviation due to the trapdoor effect may also play a role on the ΔH_{iso} and might not be exclusively be related with the CO_2 adsorption. (iii) Finally, for the Na-CHA sample, the initial ΔH_{iso} (20 kJ mol^{-1}) is significantly lower compared to the other samples. This is followed by a continuous increase in ΔH_{iso} up to a maximum of 38.3 kJ mol^{-1} at 3.4 mmol g^{-1} of CO_2 loading, then followed by a small decrease to 36.8 kJ mol^{-1} at 4.0 mmol g^{-1} loading (Fig. 5). A similar shape of the ΔH_{iso} curve has been observed for Na-Rho (however, the maximum was at half the surface coverage reported here) and, to a lesser degree, for Na-CHA samples.[7,49] The evolution of the heat of adsorption curve suggests that the surface is "homogeneous" (similar to K-CHA) with a very accessible and open micropore structure being consistent with the smaller size of the Na^+ ion.[50] The increase is thus due to the growing contribution of the adsorbate-adsorbent interactions until higher surface coverage is reached.

Based on these observations, we propose to rationalize all the heat of adsorption patterns using a general data interpretation hypothesis: It is very likely that all CO_2 adsorption data should display a so-called "bell-shaped" curve for ΔH_{iso} as a function of the surface coverages. However, depending on the chemical nature of the adsorbent and the cation, we may not be able to measure

accurately the full bell with respect to the technical and kinetic limits associated with volumetric instrumentation up to 1 bar. The substantial presence of the so-called "door-keeping" cations may also affect the ΔH_{iso} curve shape to some extent. Despite this potential effect, we consider that the general bell curve assumption holds. Therefore, the experimental position of the maximum and our ability to measure it here depends on the cation size. For Na-CHA, the small size of Na^+ cations results in adsorption of several CO_2 molecules before reaching the turning point where the loading is sufficient enough for the repulsive part of the CO_2-CO_2 contribution to be statistically dominant. While for Cs-CHA, it is the opposite case. Because Cs^+ is a large cation there is not enough room for the adsorption of many CO_2 molecules, even at low CO_2 loading, leading to an immediate impact of repulsive steric effects. In other words, with such large cations, much lower relative pressures would be necessary to see the increasing part of the bell curve. As mentioned above, the importance of the heat of adsorption component coming from the reversible molecular trapdoor effect is still unclear and will require further in-depth investigations. Finally, AP- and K-CHA represent more ideal systems where the intermediate cation size and gating effects allow for observing the "full bell". Further in-depth investigations are currently ongoing on this topic to strengthen our hypothesis. However, these investigations go beyond the scope of the present manuscript and will be reported in a dedicated high-resolution low- and high-pressure adsorption study.

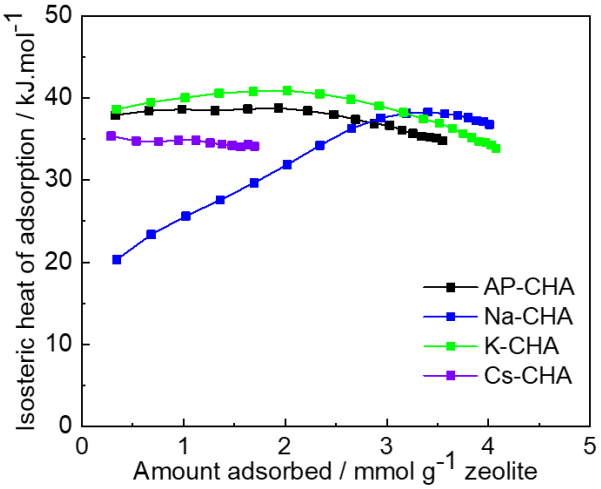

Fig. 5 Isosteric heat of adsorption of CO_2 on nanosized AP-CHA, Na-CHA, K-CHA, and Cs-CHA zeolite samples *vs* CO_2 surface loading.

To shed further light on the CO_2 adsorption behavior, the nanosized CHA samples were studied by *in situ* FTIR spectroscopy. The IR spectra of these samples under an atmosphere of CO_2 at different pressures at 298 K are presented in Fig. 6. Upon exposing the samples to CO_2, bands at

~2346 and ~2282 cm^{-1} related to physisorbed CO_2 and a series of bands from 1314 to 1734 cm^{-1} related to chemisorbed CO_2 species appear.[51,52] The band at 2346 cm^{-1} corresponds to the physisorption of $^{12}CO_2$, however, due to the high CO_2 concentration applied to all samples, a saturation of the FTIR signal prevents the utilization of this band for evaluation. As a consequence, the ^{13}C isotope (from natural abundance; 1.11 %) variant of CO_2 which can be detected by FTIR at 2282 cm^{-1} was used to quantify the physisorbed CO_2.

Upon exposing the samples in different alkali forms to CO_2, four carbonate species are detected (Fig. 6). The AP-CHA nanosized sample show a band at 1416 cm^{-1} assigned to the free carbonate species, a pair of bands at 1475 & 1595 cm^{-1} ($\Delta\upsilon_3$ = 120 cm^{-1}) assigned to unidentate carbonates, two pairs at 1349 & 1640 cm^{-1} ($\Delta\upsilon_3$ = 291 cm^{-1}) and 1380 & 1681 cm^{-1} ($\Delta\upsilon_3$ = 301 cm^{-1}) assigned to two slightly different chemisorbed bidentate carbonates species, and a pair of bands 1330 & 1720 cm^{-1} ($\Delta\upsilon_3$ = 390 cm^{-1}) related to the bridged bidentate carbonates.[51–54] Similar to the AP-CHA sample, in sample Na-CHA the formation of free carbonates at 1397 cm^{-1}, unidentate carbonates at 1431 & 1601 cm^{-1} ($\Delta\upsilon_3$ = 170 cm^{-1}), two slightly different chemisorbed bidentate carbonates species at 1349 & 1640 cm^{-1} ($\Delta\upsilon_3$ = 291 cm^{-1}) and 1381 & 1681 cm^{-1} ($\Delta\upsilon_3$ = 300 cm^{-1}), and a band at 1734 cm^{-1} assigned to bridged bidentate carbonate species are observed.[51–54] While the IR spectrum of sample K-CHA reveals the presence of free carbonate at 1422 cm^{-1}, unidentate carbonates at 1475 & 1595 cm^{-1} ($\Delta\upsilon_3$ = 120 cm^{-1}), only one type of bidentate carbonates at 1381 & 1681 cm^{-1} ($\Delta\upsilon_3$ = 300 cm^{-1}), and bridged bidentate carbonates at 1324 & 1719 cm^{-1} ($\Delta\upsilon_3$ = 395 cm^{-1}). [51–54] The IR spectrum of Cs-CHA sample shows the formation of only bidentate carbonates at 1379 & 1677 cm^{-1} ($\Delta\upsilon_3$ = 298 cm^{-1}) and bridged bidentate carbonate species at 1314 & 1720 cm^{-1} ($\Delta\upsilon_3$ = 406 cm^{-1}). [51–54] The intensity of the peaks in this region (1314 – 1734 cm^{-1}) were used to quantify the chemisorbed CO_2 species .[52]

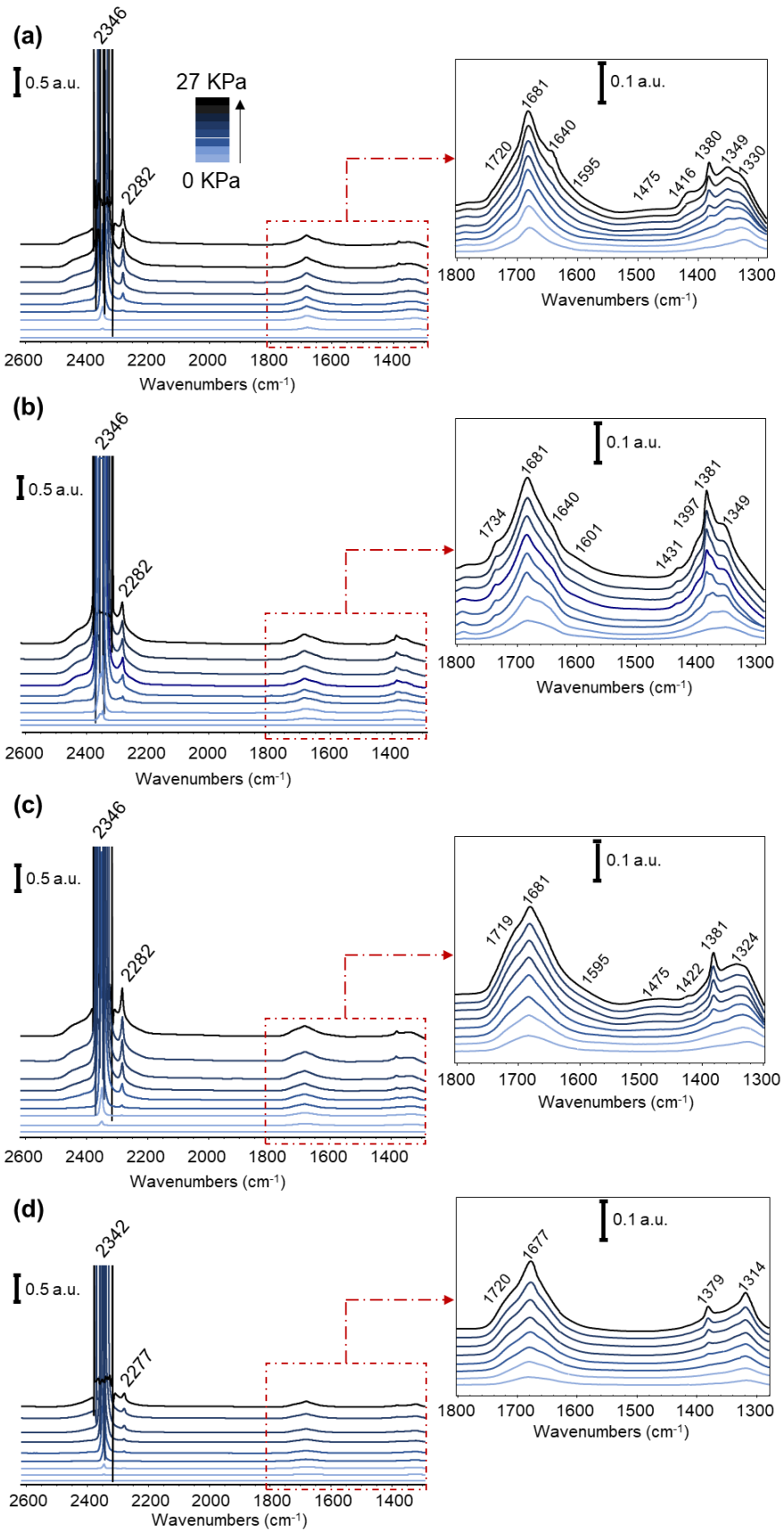

Fig. 6 *In situ* FTIR spectra of nanosized (a) AP-CHA, (b) Na-CHA, (c) K-CHA, and (d) Cs-CHA zeolite samples under increasing of CO_2 pressure (0–27 kPa) at 298 K; all samples were pretreated at 623 K under high vacuum (10^{-6} kPa) prior to measurement.

Fig. 7a shows the isotherms corresponding to physisorbed CO_2 recorded for different nanosized CHA samples at 298 K based on the integration of the $^{13}CO_2$ FTIR band at 2282 cm^{-1} which was corrected with respect to the natural abundance of ^{13}C (1.11%) to include both $^{12}CO_2$ and $^{13}CO_2$ (Table S1). Fig. 7b presents the isotherms corresponding to CO_2 chemisorption on the nanosized CHA samples at 298 K based on the FTIR chemisorption region of 1314-1734 cm^{-1} (Table S2 and Table S3). These results are consistent with the work by Polisi *et al.*[52] in studying CO_2 adsorption on sodium forms of zeolites X and Y. Moreover, these results suggest that the CO_2 chemisorption is inversely related to the size of the alkali cations. The main mode of CO_2 adsorption for the different alkali forms of nanosized CHA is physisorption since this mode consist over 96 % of the adsorption based on the *in situ* FTIR (Fig. 7a,b Table S4). This also explains the saturation of the main $^{12}CO_2$ adsorption band at 2346 cm^{-1} presented in Fig. 6 under CO_2 adsorption with pressures as low as 6 kPa.

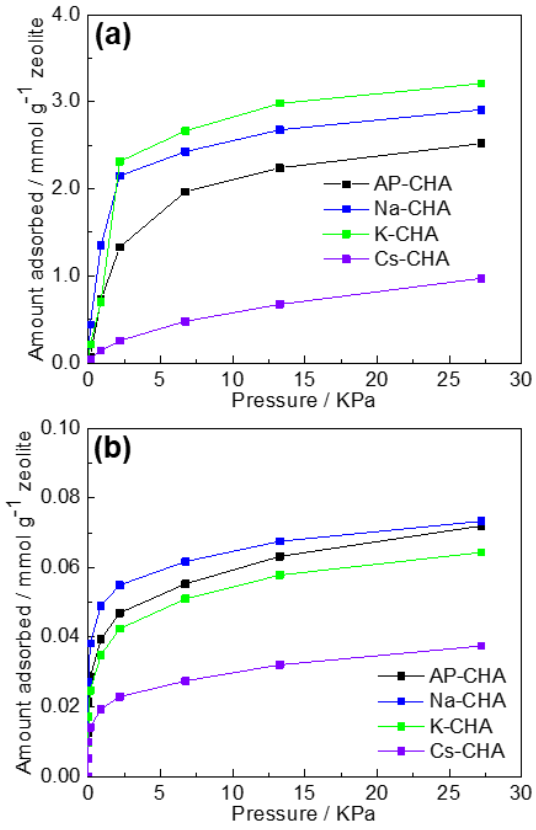

Fig. 7 CO_2 (a) physisorption and (b) chemisorption isotherms for nanosized AP-CHA, Na-CHA, K-CHA, and Cs-CHA zeolite samples based on *in situ* FTIR spectra recorded at 298 K.

Fig. 8 shows three consecutive vacuum regeneration (~ 10^{-6} KPa) and CO_2 dosing (27.2 kPa) cycles of different nanosized CHA sample recorded using *in situ* FTIR spectroscopy by integration of the $^{13}CO_2$ band at 2282 cm^{-1} corresponding to physiosorbed species corrected with respect to the

natural abundance of ^{13}C (1.11%) (Fig. 8a) and chemisorbed species in the region of 1314 – 1734 cm^{-1} (Fig. 8b). Upon applying the first vacuum (V1), all physiosorbed species are successfully removed from the samples as shown in Fig. 8a and Fig. S3. While some chemisorbed species still remain in the zeolites after regeneration using the primary vacuum (Fig. 8b and Fig. S3). The following CO_2 dosing and vacuum regeneration (P2 and V2) show that the CO_2 physisorption capacity of the samples did not change (Fig. 8a). The third CO_2 dosing (P3) reveals that the CO_2 physisorption capacity does not decrease (Fig. 8b and Fig. S3) despite the minor accumulation of the chemisorbed species. In fact, after quantification of chemisorption using *in situ* FTIR results (Table S5), this accumulation only corresponds to less than 0.8 % of the whole adsorption which is the reason why no loss of CO_2 capacity was observed.

The adsorption behavior of different alkali forms of nanosized CHA was investigated further by performing multiple thermogravimetric (TG) cycles of heating (623 K) and flowing CO_2 at 298 K (Fig. 8c). Similar to the regeneration of samples using a high vacuum, no CO_2 capacity loss was observed when heating was used for the regeneration. The XRD patterns of different alkali forms of nanosized CHA were collected after the CO_2 cycling experiments and presented in Fig. S4. The crystallinity of the samples is fully preserved thus confirming their high stability under cycling CO_2 experiments. The materials can be excellent candidates for the separation of CO_2 from N_2 or CH_4 in both vacuum swing or temperature swing processes.

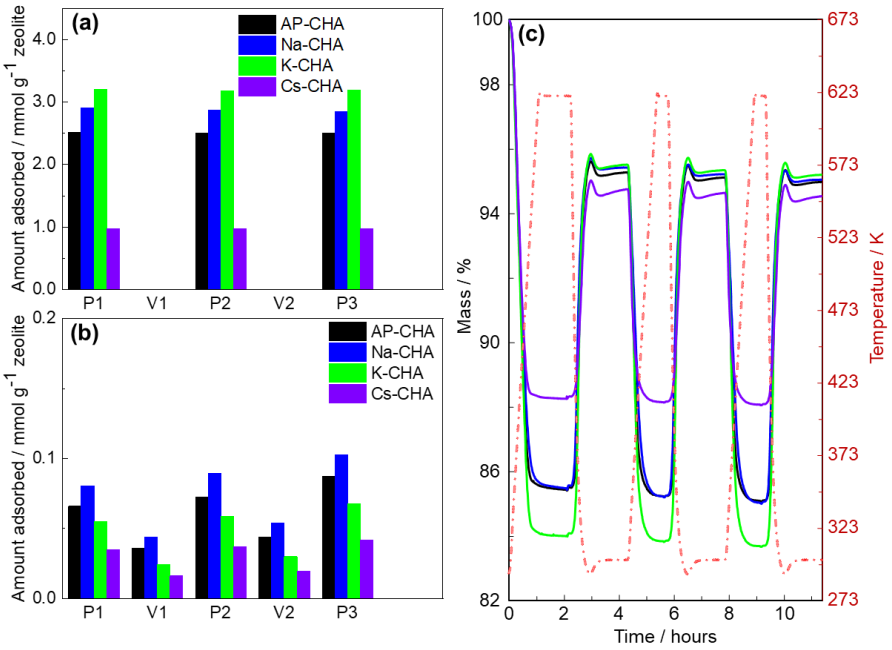

Fig. 8 Amount adsorbed CO_2 on nanosized AP-CHA, Na-CHA, K-CHA, and Cs-CHA zeolite samples under consecutive vacuum regeneration at 298 K represented by the (a) physisorbed (based on the $^{13}CO_2$ band) and (b) chemisorbed CO2 based on *in situ* FTIR at 298 K. (V) stands for high vacuum of 10^{-6} KPa and (P) stands for CO_2 dosage of 27.2 kPa, and (c) TG cycles of CO_2 adsorption under flow (40 mL min^{-1}) at 298 K and regeneration by increasing the temperature to 623 K for

The type and content of alkali metal cations (Na^+, K^+, or Cs^+) in the nanosized CHA zeolite samples significantly changes both the CO_2 adsorption behavior and the CO_2 separation performance in the presence of N_2. This is due to the different sizes of the cations which dictates their ability to occupy the 8MRs and control the selective uptake of CO_2 in the presence of non-polar small molecules such as N_2 and CH_4. For the nanosized Na-CHA sample, the micropore volume based on N_2 adsorption at 77 K (0.14 $cm^3\ g^{-1}$ at 77 K, Table 3) as well as the high CO_2 adsorption capacity (4.0 mmol g^{-1} at 298 K, Fig. 3c) are consistent with the previously published results for micron-sized Na-CHA. The results show that Na^+ is unable to effectively occupy the 8MRs of the supercages and to control the selective adsorption of small molecules.[24] Hence, an open porosity can be imagined for this sample which can be further supported by the ΔH_{iso} results (Fig. 5) with a wide range of adsorption sites with different energies being available. Conversely, in the nanosized AP-CHA and K-CHA samples, molecular trapdoor behavior is observed due to the extremely low micropore volume in the presence of N_2 (0.01 $cm^3\ g^{-1}$, Table 3) while possessing high CO_2 capacity (Fig. 3). The nanosized Cs-CHA sample shows similar behavior to the K-CHA sample, however, the CO_2 capacity is lower (1.7 mmol g^{-1} at 298 K, Fig. 3c) due to the larger size of the Cs^+ cation. Comparing the CO_2 adsorption isotherms obtained from the adsorption measurements and from *in situ* FTIR spectroscopy (Fig. 3c *vs* Fig. 7a), one can conclude that all samples mainly contained physisorbed CO_2 (over 96 % of the CO_2 adsorption) with minor formation of carbonate species (Fig. 6).

4. Conclusions

The adsorption of CO_2 in four different alkali metal cationic forms of nanosized chabazite (CHA) zeolite (AP-, Na, K-, and Cs-CHA) were studied using GCMC modeling, experimental adsorption isotherm measurements, isosteric heat of adsorption calculations and *in situ* FTIR spectroscopy. Comparing GCMC predictions for CO_2 adsorption isotherms with those obtained experimentally for the different alkali metal cationic forms of nanosized CHA samples revealed that this method is a powerful tool to predict the CO_2 adsorption capacity of different CHA samples with various cationic compositions where diffusion restrictions of guest molecules due to the size of the extra-framework cations are not foreseen. Experimental adsorption measurements showed that the Na^+ cations in nanosized Na-CHA sample do not block the CHA pore openings (8MRs) to guest molecules (CO_2 or N_2). The Na-CHA sample exhibits an open porosity in contrast to the other samples. This samples shows high CO_2 uptake (4.5 mmol g^{-1} at 60 KPa and 273 K) and high micropore volume upon N_2 adsorption (0.14 $cm^3\ g^{-1}$ at 77 K) which is similar to micron-sized zeolites with comparable Si/Al ratios and cation populations. In comparison, the nanosized K-CHA

sample shows a high CO_2 adsorption capacity (4.5 mmol g^{-1} at 60 KPa and 273 K) and significantly lower micropore volume based on N_2 adsorption measurements (0.01 cm^3 g^{-1} at 77 K), hence molecular trapdoor behavior is observed for this sample. Similar to the K-CHA sample, the nanosized Cs-CHA sample shows negligible N_2 adsorption (0.01 cm^3 g^{-1}), however, the CO_2 capacity decreases by half (2.1 mmol g^{-1} *vs* 4.5 mmol g^{-1}) compared to the K-CHA sample due to the larger size of the Cs^+ cations and the restricted diffusion of guest molecules. A general bell-shaped model is proposed for the isosteric heat of CO_2 adsorption with the position of the curve maximum and extent of each part of the bell curve being dependent on the nature of the cations. Moreover, *in situ* FTIR CO_2 adsorption results revealed that CO_2 is mainly physically adsorbed on all nanosized CHA sample, and the chemisorption of CO_2 can be decreased by exchanging smaller for larger cations. The CHA nanocrystals may be considered as an excellent candidate for CO_2 capture from a mixture containing N_2 and possibly CH_4 in vacuum swing (especially for low-temperature regeneration processes) or temperature swing applications.

Author Contributions

S. G.: synthesis, analysis, validation, visualization, writing of original draft, review & editing; B. C.: theoretical study, supervision of theoretical section, validation, writing – review & editing; E. B. C.: validation, writing – review & editing; R. G. N.: analysis, methodology, validation, writing – review & editing; P. B.: investigation, validation, supervision of the FTIR section; M. D.: analysis; L. J. A.: analysis; V. R.: analysis; S. M.: funding acquisition, project administration, resources, supervision of the whole work, validation, writing – review & editing

Conflicts of interest

There are no conflicts to declare.

Acknowledgement

Financial support from the Normandy Region through the RIN Recherche Program (grant 18P01675) is acknowledged. Numerical simulations were performed using the Froggy platform of the GRICAD infrastructure (https://gricad.univ-grenoble-alpes.fr), which is supported by the Rhone-Alpes region (GRANT CPER07-13 CIRA) and the Equip@Meso project (reference ANR-10-EQPX-29-01) of the programme Investissements d'Avenir supervised by the French National Research Agency.

5. References

(1) Tomé, L. C.; Marrucho, I. M. Ionic Liquid-Based Materials: A Platform to Design Engineered CO2 Separation Membranes. *Chem. Soc. Rev.* **2016**, *45* (10), 2785–2824. https://doi.org/10.1039/C5CS00510H.

(2) Pachauri, R. K. et al. *Climate Change 2014: Synthesis Report. Contribution of Working Groups I, II and III to the Fifth Assessment Report of the Intergovernmental Panel on Climate Change*; IPCC: Geneva, Switzerland, 2014.

(3) Kenarsari, S. D.; Yang, D.; Jiang, G.; Zhang, S.; Wang, J.; Russell, A. G.; Wei, Q.; Fan, M. Review of Recent Advances in Carbon Dioxide Separation and Capture. *RSC Adv.* **2013**, *3* (45), 22739–22773. https://doi.org/10.1039/C3RA43965H.

(4) Khalilpour, R.; Mumford, K.; Zhai, H.; Abbas, A.; Stevens, G.; Rubin, E. S. Membrane-Based Carbon Capture from Flue Gas: A Review. *J. Clean. Prod.* **2015**, *103*, 286–300. https://doi.org/10.1016/j.jclepro.2014.10.050.

(5) Brunetti, A.; Drioli, E.; Lee, Y. M.; Barbieri, G. Engineering Evaluation of CO2 Separation by Membrane Gas Separation Systems. *J. Membr. Sci.* **2014**, *454*, 305–315. https://doi.org/10.1016/j.memsci.2013.12.037.

(6) Spigarelli, B. P.; Kawatra, S. K. Opportunities and Challenges in Carbon Dioxide Capture. *J. CO2 Util.* **2013**, *1*, 69–87. https://doi.org/10.1016/j.jcou.2013.03.002.

(7) Zhang, J.; Singh, R.; Webley, P. A. Alkali and Alkaline-Earth Cation Exchanged Chabazite Zeolites for Adsorption Based CO2 Capture. *Microporous Mesoporous Mater.* **2008**, *111* (1), 478–487. https://doi.org/10.1016/j.micromeso.2007.08.022.

(8) Slater, A. G.; Cooper, A. I. Function-Led Design of New Porous Materials. *Science* **2015**, *348* (6238), aaa8075. https://doi.org/10.1126/science.aaa8075.

(9) Palomino, M.; Corma, A.; Rey, F.; Valencia, S. New Insights on CO2−Methane Separation Using LTA Zeolites with Different Si/Al Ratios and a First Comparison with MOFs. *Langmuir* **2010**, *26* (3), 1910–1917. https://doi.org/10.1021/la9026656.

(10) Sumida, K.; Rogow, D. L.; Mason, J. A.; McDonald, T. M.; Bloch, E. D.; Herm, Z. R.; Bae, T.-H.; Long, J. R. Carbon Dioxide Capture in Metal–Organic Frameworks. *Chem. Rev.* **2012**, *112* (2), 724–781. https://doi.org/10.1021/cr2003272.

(11) Rochelle, G. T. Amine Scrubbing for CO2 Capture. *Science* **2009**, *325* (5948), 1652–1654. https://doi.org/10.1126/science.1176731.

(12) Bae, Y.-S.; Snurr, R. Q. Development and Evaluation of Porous Materials for Carbon Dioxide Separation and Capture. *Angew. Chem. Int. Ed.* **2011**, *50* (49), 11586–11596. https://doi.org/10.1002/anie.201101891.

(13) Choi, H. J.; Jo, D.; Min, J. G.; Hong, S. B. The Origin of Selective Adsorption of CO2 on Merlinoite Zeolites. *Angew. Chem. Int. Ed.* **2021**, *60* (8), 4307–4314. https://doi.org/10.1002/anie.202012953.

(14) Díaz, E.; Muñoz, E.; Vega, A.; Ordóñez, S. Enhancement of the CO2 Retention Capacity of Y Zeolites by Na and Cs Treatments: Effect of Adsorption Temperature and Water Treatment. *Ind. Eng. Chem. Res.* **2008**, *47* (2), 412–418. https://doi.org/10.1021/ie070685c.

(15) Tosheva, L.; Valtchev, V. P. Nanozeolites: Synthesis, Crystallization Mechanism, and Applications. *Chem. Mater.* **2005**, *17* (10), 2494–2513. https://doi.org/10.1021/cm047908z.

(16) Mintova, S.; Grand, J.; Valtchev, V. Nanosized Zeolites: Quo Vadis? *Comptes Rendus Chim.* **2016**, *19* (1), 183–191. https://doi.org/10.1016/j.crci.2015.11.005.

(17) Mintova, S.; Gilson, J.-P.; Valtchev, V. Advances in Nanosized Zeolites. *Nanoscale* **2013**, *5* (15), 6693–6703. https://doi.org/10.1039/C3NR01629C.

(18) Vuong, G.-T.; Do, T.-O. Nanozeolites and Nanoporous Zeolitic Composites: Synthesis and Applications. In *Mesoporous Zeolites*; John Wiley & Sons, Ltd, 2015; pp 79–114. https://doi.org/10.1002/9783527673957.ch3.

(19) Dusselier, M.; Davis, M. E. Small-Pore Zeolites: Synthesis and Catalysis. *Chem. Rev.* **2018**, *118* (11), 5265–5329. https://doi.org/10.1021/acs.chemrev.7b00738.

(20) Cheung, O.; Hedin, N. Zeolites and Related Sorbents with Narrow Pores for CO2 Separation from Flue Gas. *RSC Adv.* **2014**, *4* (28), 14480–14494. https://doi.org/10.1039/C3RA48052F.
(21) Lozinska, M. M.; Mangano, E.; Greenaway, A. G.; Fletcher, R.; Thompson, S. P.; Murray, C. A.; Brandani, S.; Wright, P. A. Cation Control of Molecular Sieving by Flexible Li-Containing Zeolite Rho. *J. Phys. Chem. C* **2016**, *120* (35), 19652–19662. https://doi.org/10.1021/acs.jpcc.6b04837.
(22) Georgieva, V. M.; Bruce, E. L.; Verbraeken, M. C.; Scott, A. R.; Casteel, W. J.; Brandani, S.; Wright, P. A. Triggered Gate Opening and Breathing Effects during Selective CO2 Adsorption by Merlinoite Zeolite. *J. Am. Chem. Soc.* **2019**, *141* (32), 12744–12759. https://doi.org/10.1021/jacs.9b05539.
(23) Shang, J.; Li, G.; Singh, R.; Gu, Q.; Nairn, K. M.; Bastow, T. J.; Medhekar, N.; Doherty, C. M.; Hill, A. J.; Liu, J. Z.; Webley, P. A. Discriminative Separation of Gases by a “Molecular Trapdoor” Mechanism in Chabazite Zeolites. *J. Am. Chem. Soc.* **2012**, *134* (46), 19246–19253. https://doi.org/10.1021/ja309274y.
(24) Shang, J.; Li, G.; Singh, R.; Xiao, P.; Liu, J. Z.; Webley, P. A. Determination of Composition Range for “Molecular Trapdoor” Effect in Chabazite Zeolite. *J. Phys. Chem. C* **2013**, *117* (24), 12841–12847. https://doi.org/10.1021/jp4015146.
(25) Lozinska, M. M.; Mangano, E.; Mowat, J. P. S.; Shepherd, A. M.; Howe, R. F.; Thompson, S. P.; Parker, J. E.; Brandani, S.; Wright, P. A. Understanding Carbon Dioxide Adsorption on Univalent Cation Forms of the Flexible Zeolite Rho at Conditions Relevant to Carbon Capture from Flue Gases. *J. Am. Chem. Soc.* **2012**, *134* (42), 17628–17642. https://doi.org/10.1021/ja3070864.
(26) Li, G. (Kevin); Shang, J.; Gu, Q.; Awati, R. V.; Jensen, N.; Grant, A.; Zhang, X.; Sholl, D. S.; Liu, J. Z.; Webley, P. A.; May, E. F. Temperature-Regulated Guest Admission and Release in Microporous Materials. *Nat. Commun.* **2017**, *8* (1), 1–9. https://doi.org/10.1038/ncomms15777.
(27) Debost, M.; Klar, P. B.; Barrier, N.; Clatworthy, E. B.; Grand, J.; Lainé, F.; Brazda, P.; Palatinus, L.; Nesterenko, N.; Boullay, P.; Mintova, S. Synthesis of Discrete CHA Zeolite Nanocrystals without Organic Templates for Selective CO2 Capture. *Angew. Chem. n/a* (n/a). https://doi.org/10.1002/ange.202009397.
(28) Shang, J.; Li, G.; Singh, R.; Xiao, P.; Danaci, D.; Liu, J. Z.; Webley, P. A. Adsorption of CO2, N2, and CH4 in Cs-Exchanged Chabazite: A Combination of van Der Waals Density Functional Theory Calculations and Experiment Study. *J. Chem. Phys.* **2014**, *140* (8), 084705. https://doi.org/10.1063/1.4866455.
(29) Shang, J.; Li, G.; Webley, P. A.; Liu, J. Z. A Density Functional Theory Study for the Adsorption of Various Gases on a Caesium-Exchanged Trapdoor Chabazite. *Comput. Mater. Sci.* **2016**, *122*, 307–313. https://doi.org/10.1016/j.commatsci.2016.05.040.
(30) Ghojavand, S.; Clatworthy, E. B.; Vicente, A.; Dib, E.; Ruaux, V.; Debost, M.; El Fallah, J.; Mintova, S. The Role of Mixed Alkali Metal Cations on the Formation of Nanosized CHA Zeolite from Colloidal Precursor Suspension. *J. Colloid Interface Sci.* **2021**, *604*, 350–357. https://doi.org/10.1016/j.jcis.2021.06.176.
(31) Rouquerol, J.; Llewellyn, P.; Rouquerol, F. Is the Bet Equation Applicable to Microporous Adsorbents? In *Studies in Surface Science and Catalysis*; Elsevier, 2007; Vol. 160, pp 49–56. https://doi.org/10.1016/S0167-2991(07)80008-5.
(32) Yang, S.-T.; Kim, J.; Ahn, W.-S. CO2 Adsorption over Ion-Exchanged Zeolite Beta with Alkali and Alkaline Earth Metal Ions. *Microporous Mesoporous Mater.* **2010**, *135* (1), 90–94. https://doi.org/10.1016/j.micromeso.2010.06.015.
(33) Mousavi, H.; Towfighi Darian, J.; Mokhtarani, B. Enhanced Nitrogen Adsorption Capacity on Ca2+ Ion-Exchanged Hierarchical X Zeolite. *Sep. Purif. Technol.* **2021**, *264*, 118442. https://doi.org/10.1016/j.seppur.2021.118442.
(34) Zholobenko, V.; Freitas, C.; Jendrlin, M.; Bazin, P.; Travert, A.; Thibault-Starzyk, F. Probing the Acid Sites of Zeolites with Pyridine: Quantitative AGIR Measurements of the Molar Absorption Coefficients. *J. Catal.* **2020**, *385*, 52–60. https://doi.org/10.1016/j.jcat.2020.03.003.

(35) Ni, H.; Keppler, H. Carbon in Silicate Melts. *Rev. Mineral. Geochem.* **2013**, *75* (1), 251–287. https://doi.org/10.2138/rmg.2013.75.9.
(36) Dixon, J. E.; Pan, V. Determination of the Molar Absorptivity of Dissolved Carbonate in Basanitic Glass. *Am. Mineral.* **1995**, *80* (11–12), 1339–1342. https://doi.org/10.2138/am-1995-11-1224.
(37) Coasne, B.; Galarneau, A.; Gerardin, C.; Fajula, F.; Villemot, F. Molecular Simulation of Adsorption and Transport in Hierarchical Porous Materials. *Langmuir* **2013**, *29* (25), 7864–7875. https://doi.org/10.1021/la401228k.
(38) Ho, L. N.; Schuurman, Y.; Farrusseng, D.; Coasne, B. Solubility of Gases in Water Confined in Nanoporous Materials: ZSM-5, MCM-41, and MIL-100. *J. Phys. Chem. C* **2015**, *119* (37), 21547–21554. https://doi.org/10.1021/acs.jpcc.5b06660.
(39) Loewenstein, W. The Distribution of Aluminum in the Tetrahedra of Silicates and Aluminates. *Am. Mineral.* **1954**, *39* (1–2), 92–96.
(40) Jeffroy, M.; Boutin, A.; Fuchs, A. H. Understanding the Equilibrium Ion Exchange Properties in Faujasite Zeolite from Monte Carlo Simulations. *J. Phys. Chem. B* **2011**, *115* (50), 15059–15066. https://doi.org/10.1021/jp209067n.
(41) Powder Pattern Identification Table. In *Collection of Simulated XRD Powder Patterns for Zeolites (Fifth Edition)*; Treacy, M. M. J., Higgins, J. B., Eds.; Elsevier Science B.V.: Amsterdam, 2007; pp 10–16. https://doi.org/10.1016/B978-044453067-7/50473-1.
(42) Panezai, H.; Fan, M.; Sun, J.; Bai, S.; Wu, X. Influence of Ca2+ or Na+ Extraframework Cations on the Thermal Dehydration and Related Kinetic Performance of LSX Zeolite. *J. Phys. Chem. Solids* **2016**, *99*, 1–10. https://doi.org/10.1016/j.jpcs.2016.07.025.
(43) Hayamizu, K.; Chiba, Y.; Haishi, T. Dynamic Ionic Radius of Alkali Metal Ions in Aqueous Solution: A Pulsed-Field Gradient NMR Study. *RSC Adv.* **2021**, *11* (33), 20252–20257. https://doi.org/10.1039/D1RA02301B.
(44) Calligaris, M.; Mezzetti, A.; Nardin, G.; Randaccio, L. Crystal Structures of the Hydrated and Dehydrated Forms of a Partially Cesium-Exchanged Chabazite. *Zeolites* **1986**, *6* (2), 137–141. https://doi.org/10.1016/S0144-2449(86)80012-4.
(45) Ridha, F. N.; Webley, P. A. Anomalous Henry's Law Behavior of Nitrogen and Carbon Dioxide Adsorption on Alkali-Exchanged Chabazite Zeolites. *Sep. Purif. Technol.* **2009**, *67* (3), 336–343. https://doi.org/10.1016/j.seppur.2009.03.045.
(46) Smith, L. J.; Eckert, H.; Cheetham, A. K. Site Preferences in the Mixed Cation Zeolite, Li,Na-Chabazite: A Combined Solid-State NMR and Neutron Diffraction Study. *J. Am. Chem. Soc.* **2000**, *122* (8), 1700–1708. https://doi.org/10.1021/ja992882b.
(47) Orsikowsky-Sanchez, A.; Plantier, F.; Miqueu, C. Coupled Gravimetric, Manometric and Calorimetric Study of CO2, N2 and CH4 Adsorption on Zeolites for the Assessment of Classical Equilibrium Models. *Adsorption* **2020**, *26* (7), 1137–1152. https://doi.org/10.1007/s10450-020-00206-7.
(48) Pham, T. D.; Hudson, M. R.; Brown, C. M.; Lobo, R. F. Molecular Basis for the High CO2 Adsorption Capacity of Chabazite Zeolites. *ChemSusChem* **2014**, *7* (11), 3031–3038. https://doi.org/10.1002/cssc.201402555.
(49) Lozinska, M. M.; Mowat, J. P. S.; Wright, P. A.; Thompson, S. P.; Jorda, J. L.; Palomino, M.; Valencia, S.; Rey, F. Cation Gating and Relocation during the Highly Selective "Trapdoor" Adsorption of CO2 on Univalent Cation Forms of Zeolite Rho. *Chem. Mater.* **2014**, *26* (6), 2052–2061. https://doi.org/10.1021/cm404028f.
(50) Cimino, R. T.; Kowalczyk, P.; Ravikovitch, P. I.; Neimark, A. V. Determination of Isosteric Heat of Adsorption by Quenched Solid Density Functional Theory. *Langmuir* **2017**, *33* (8), 1769–1779. https://doi.org/10.1021/acs.langmuir.6b04119.
(51) Stevens, R. W.; Siriwardane, R. V.; Logan, J. In Situ Fourier Transform Infrared (FTIR) Investigation of CO2 Adsorption onto Zeolite Materials. *Energy Fuels* **2008**, *22* (5), 3070–3079. https://doi.org/10.1021/ef800209a.
(52) Polisi, M.; Grand, J.; Arletti, R.; Barrier, N.; Komaty, S.; Zaarour, M.; Mintova, S.; Vezzalini, G. CO2 Adsorption/Desorption in FAU Zeolite Nanocrystals: In Situ

Synchrotron X-Ray Powder Diffraction and in Situ Fourier Transform Infrared Spectroscopic Study. *J. Phys. Chem. C* **2019**, *123* (4), 2361–2369. https://doi.org/10.1021/acs.jpcc.8b11811.

(53) Du, H.; Williams, C. T.; Ebner, A. D.; Ritter, J. A. In Situ FTIR Spectroscopic Analysis of Carbonate Transformations during Adsorption and Desorption of CO2 in K-Promoted HTlc. *Chem. Mater.* **2010**, *22* (11), 3519–3526. https://doi.org/10.1021/cm100703e.

(54) Coenen, K.; Gallucci, F.; Mezari, B.; Hensen, E.; van Sint Annaland, M. An In-Situ IR Study on the Adsorption of CO2 and H2O on Hydrotalcites. *J. CO2 Util.* **2018**, *24*, 228–239. https://doi.org/10.1016/j.jcou.2018.01.008.